Solar cells based on n^+-AZO/p-$BaSi_2$ heterojunction
Advanced opto-electrical modelling and experimental demonstration

Yamashita, Yudai; Ruiz Tobon, Carlos Mario; Santbergen, Rudi; Zeman, Miro; Isabella, Olindo; Suemasu, Takashi

DOI
10.1016/j.solmat.2021.111181

Publication date
2021

Document Version
Accepted author manuscript

Published in
Solar Energy Materials and Solar Cells

Solar cells based on n^+-AZO/p-$BaSi_2$ heterojunction: advanced opto-electrical modelling and experimental demonstration

Yudai Yamashita[1], Carlos Mario Ruiz Tobon[2], Rudi Santbergen[2], Miro Zeman[2], Olindo Isabella[2], Takashi Suemasu[3]

[1]*Graduate School of Pure and Applied Sciences, University of Tsukuba, Tsukuba, Ibaraki 305-8573, Japan*
[2]*Delft University of Technology, Photovoltaic Materials and Devices group, Mekelweg 4, 2628 CD Delft, the Netherlands*
[3]*Department of Applied Physics, Faculty of Pure and Applied Sciences, University of Tsukuba, Tsukuba, Ibaraki 305-8573, Japan*

We performed advanced opto-electrical simulations on thin-film $BaSi_2$ solar cells. First, absorption spectra of $BaSi_2$-pn homojunction solar cells on Si substrate were calculated based on flat and/or pyramidally-textured surfaces, wherein 20-nm-thick n^+-$BaSi_2$ was the topmost electron transport layer. By changing the front surface structure from flat to texture, the reflectance decreased in the wavelength (λ) range 700 – 1200 nm and the photocurrent density (J_{ph}) delivered by the photogenerated carriers in the 500-nm thick p-$BaSi_2$ layer increased by 1.2 mA/cm^2. Simulations revealed that the key factor inhibiting light absorption in the p-$BaSi_2$ layer was parasitic absorption in the n^+-$BaSi_2$ and in the c-Si substrate. To solve these optical issues, we propose a new device structure, Al-doped n^+-ZnO (AZO, 50 nm)/i-ZnO (20 nm)/p-$BaSi_2$ (500 nm) heterojunction solar cell (HJSC). In this device structure, the parasitic absorption reduced drastically, and J_{ph} reached 30.23 mA/cm^2. Furthermore, by replacing the Si substrate with a glass substrate, the light trapping worked more effectively, and the absorber layer thickness required for J_{ph} to saturate was reduced to 1 μm, yielding 32.06 mA/cm^2. Based on these simulation results, we manufactured n^+-AZO/p-$BaSi_2$ HJSC. The internal quantum efficiency exceeded 30% at λ = 600 nm, meaning that we demonstrated the operation of n^+-AZO/p-$BaSi_2$ HJSC for the first time. We investigated origins of small efficiencies compared to those simulated, and found that the passivation of defects in the p-$BaSi_2$ layer and the reduction of carrier recombination at the i-ZnO/p-$BaSi_2$ interface would significantly improve the solar cell performance.

I. INTRODUCTION

Thin-film solar cells (TFSCs), such as III-V [1,2], CIGS [3], perovskite [4-6], CdTe [7,8], and others [9,10] have been developed to achieve high power conversion efficiency (η). However, large-scale deployment of these solar cells equivalent to crystalline Si (c-Si) solar cells is not easy because the materials used in TFSCs contain non-abundant and/or toxic elements. Hence, there is a special need for alternative thin-film materials for photovoltaic (PV) applications. Under such circumstances, we have focused on semiconducting barium disilicide ($BaSi_2$) as a new material for TFSCs [11]. It has a suitable bandgap (E_g) of 1.3 eV, a large optical absorption coefficient of 3×10^4 cm^{-1} for a photon energy of 1.5 eV (more than 40 times larger than that of c-Si), and excellent minority-carrier properties [12–16]. Furthermore, it is composed of only safe, stable, and earth-abundant elements. $BaSi_2$ has a small lattice mismatch with Si(111), i.e., 0.1% and 1.1% along the *b*- and *c*-axes, respectively, allowing for epitaxial growth on an inexpensive Si substrate [17]. For these reasons, $BaSi_2$ is considered to be a promising material for terawatt-class power generation. We have achieved η values approaching 10% in p^+-$BaSi_2$/n-Si heterojunction solar cells (HJSCs) without any special treatment for passivation [18–20], wherein the depletion region stretched toward the n-Si side and therefore most of the photons were absorbed in the n-Si region. Our next target is $BaSi_2$-pn homojunction solar cells (SCs), for which η is expected to exceed 25% according to calculations (Fig. 1) [21]. Furthermore, $BaSi_2$ PV technology could be applied to Si-based tandem solar cells by expanding its E_g via alloying $BaSi_2$ with C [22]. Currently, we focus on further improvement of the optical and transport properties of $BaSi_2$ films. For this purpose, we have used photoresponsivity as a measure to find optimum growth conditions for light absorber layers. In recent years, the photoresponsivity of $BaSi_2$ films has increased drastically due to elevated substrate temperatures during thin-film growth [23], three-step growth [24], lightly B-/As-doping [25,26] and H-passivation [27–30] to passivate Si vacancies (V_{Si}), reaching ~1 A/W at 800 nm under a bias voltage of 0.1 V between the front surface and back surface electrodes.

However, even with such high-quality $BaSi_2$ light absorber layers, the η of $BaSi_2$-pn SCs was quite small (η = 0.28%) [31], and the reason for this remains unclear. We therefore suppose that the extraction of photogenerated carriers is somehow hindered in the solar cell device structures. In fact, our previous research showed that the external quantum efficiency (*EQE*) in the short wavelength region is as low as 40% [32]. The structural design of solar cells is very important in achieving high η. For Si solar cells, devices with various structures such as heterojunction with intrinsic thin-layer (HIT) solar cells [33-36], tunnel oxide passivated contact (TOPCon) solar cells [37-41], and passivated emitter and rear cell (PERC) solar cells [42] have been studied for years and their transport mechanisms unveiled [43,44]. In this study, we firstly aimed to clarify the factors that reduce the η in $BaSi_2$-pn SCs by advanced opto-electrical modelling. Simulation results are an important tool for solar cell design, as they provide, as in this study, detailed insight in reflection and parasitic absorption losses as well as recombination mechanisms which degrade $BaSi_2$-pn SCs performance. We therefore proposed a new device structure, Al-doped n^+-ZnO (AZO)/p-$BaSi_2$ HJSC. With this device structure we address both previous optical and electrical shortcomings and show a pathway for reaching efficiencies well above 20%. In the last part of our contribution, we report on the first experimental demonstration of n^+-AZO/p-$BaSi_2$ HJSC.

2. METHODS

2.1 Simulation Method

In this study, we performed optical simulations using the GENPRO4 [45] software and electrical simulation using ASA [46,47] version 7 (ASA-7), both developed at the Delft University of Technology. The complex refractive index (n + ik) of each layer was measured independently as a function of wavelength (λ) using spectroscopic ellipsometry (see Fig. 2) and was used as an input. Note that the extinction coefficient k of both p-$BaSi_2$ and p^+-$BaSi_2$ materials was set to zero for wavelengths longer than 950 nm. This complies with the experimental evidence of

absence of photoresponsivity signal in such materials for $\lambda > 950$ nm [48]. By integrating the resulting absorption spectra of $BaSi_2$ light absorber layers over the AM1.5 spectrum range, the related photocurrent density J_{ph} values were obtained.

Optically, we investigated $BaSi_2$-pn SCs structure: ITO (80 nm) / a-Si (3 nm) / n^+-$BaSi_2$ (20 nm) / p-$BaSi_2$ (500 nm) / p^+-$BaSi_2$ (20 nm) / Si substrate (500 μm) / Ag (100 nm), which is the same as the layered structure used for the first demonstration of $BaSi_2$-pn SCs [31]. In this work, next to simulating flat interfaces, we also introduced the typical 3D pyramidal texture at front and/or back surfaces of the Si substrate to investigate the anti-reflection and light trapping effects. For this purpose, an atomic force microscopy image of a pyramid-type texture obtained by chemical-etching of a Si substrate was used (see Fig. 2(c)). In addition, to increase light absorption in $BaSi_2$ light absorber layers, we investigated n^+-AZO/p-$BaSi_2$ HJSCs, in which the electron transport layer (ETL) was changed from n^+-$BaSi_2$ to more transparent n^+-AZO and the substrate was also eventually changed from Si to glass. The ZnO-based ETL was set as AZO (50 nm) / ZnO (20 nm).

For the electrical modelling, the generation rate provided by GENPRO4 was combined with ASA-7 software, which solves the semiconductor equations including bulk and surficial recombination mechanisms [49] as well as advanced transport mechanisms such as non-local tunneling currents [50], band-to-band tunneling [51] and trap-assisted tunneling [52,53]. suitable for both single- and multi-junction devices.

2.2 Experimental Method

An ion-pumped molecular beam epitaxy (MBE) system equipped with an electron-beam gun for high-purity (10N) Si and standard Knudsen cells for low-purity (3N) Ba and 3N-B was used. We used B-implanted p-Si(111) substrates (resistivity $\rho = 1 – 4$ Ωcm) with a dose of 2.5×10^{14} cm^{-2}. A projected range was set at 50 nm so that the hole concentration p would be approximately 2×10^{19} cm^{-3} on the surface after activation annealing at 900 °C for 3 min.

Before growing the films, the Si substrates were cleaned by the standard RCA procedure, followed by thermal cleaning at 900 °C for 30 min in an ultra-high vacuum chamber to remove the protective oxide layer from the surface. For epitaxial growth of $BaSi_2$ films, we evaporated Ba onto the heated Si substrate at a substrate temperature of T_S = 500 °C to form a 5-nm-thick $BaSi_2$ template layer by reactive deposition epitaxy (RDE). This layer acts as a seed for the growth of subsequent layers [54]. In the RDE process, the Ba deposition rate was fixed at 1 nm/min. Next, we formed a stack of heavily B-doped p^+-$BaSi_2$ (20 nm) / lightly B-doped p-$BaSi_2$ (500 nm) by MBE. The p of these layers was 2.0×10^{19} and 1×10^{17} cm^{-3}, respectively, at room temperature (RT). Finally, a 3-nm-thick amorphous Si (a-Si) layer was deposited *in-situ* on the surface at 180 °C. The a-Si layer prevents oxidation of the $BaSi_2$ surface [55] and does not hinder carrier transport across the a-Si/$BaSi_2$ interface [56-58]. After exposing the sample to air to load it into another chamber for sputtering, 50-nm-thick ZnO and 300-nm-thick AZO with a diameter of 1 mm were fabricated on the front surface at 150 °C by sputtering and Al electrodes were used on the back side. The electron concentration of ZnO and AZO were $n \sim 10^{15}$ and 10^{20} cm^{-3}, respectively, at RT.

Solar cell performance was evaluated using a mask with a 1-mm-diameter hole under AM 1.5 conditions at 25 °C. Photoresponse and reflectance spectra were evaluated using a lock-in technique with a xenon lamp (150 W) and a single monochromator with a focal-length of 25 cm (Bunko Keiki SM-1700A and RU-60N). The light intensity was calibrated using a pyroelectric sensor (Melles Griot 13PEM001/J).

3. RESULTS AND DISCUSSION

3.1 Effect of textured surfaces on the photocurrent of $BaSi_2$-pn SCs

As shown in Fig. 3, four types of solar cell structures were simulated, namely, “Flat/Flat” structure with flat surfaces on both sides, “Texture/Flat” structure with texture only on the front side, “Flat/Texture” structure with texture only on the back side, and “Texture/Texture”

structure with both sides textured. By changing the front surface structure from flat to textured (see Fig. 3(b)), the reflectance reduced in the λ range 700 – 1200 nm compared to that in Fig. 3(a), and the J_{ph} increased by 1.2 mA/cm^2. On the other hand, the light trapping effect by the rear texture structure was not pronounced as shown in Fig. 3(c,d). This is probably because almost all the transmitted light was absorbed by the Si substrate before bouncing back to the p-$BaSi_2$ layers. In addition, it was found that the key factor inhibiting light coupling in the p-$BaSi_2$ layer was the parasitic absorption in the n^+-$BaSi_2$ ETL. This parasitic absorption is unavoidable when $BaSi_2$ is used for ETL as the sunny side, because $BaSi_2$ has higher light absorption coefficients than CIGS.[12]

3.2 Simulation of n^+-AZO/p-$BaSi_2$ HJSCs

Extensively studied TFSCs, e.g. CIGS, CdTe are a kind of HJSCs which consist of p-type absorber layers and n-type window layers. The wide E_g of the window layer allows more photons to reach the absorber layer. Another advantage of a heterojunction solar cell is that the recombination in the wide E_g window layer is lower than that of a homojunction solar cell. Based on these arguments, we proposed n^+-AZO/p-$BaSi_2$ HJSCs in which the n^+-$BaSi_2$ ETL was replaced with n^+-AZO layers. Figure 4 shows the schematic and the band diagram of n^+-AZO/p-$BaSi_2$ HJSCs.

Figures 5(a,b) show the absorption spectra of the n^+-AZO/p-$BaSi_2$ HJSCs with (a) Flat/Flat and (b) Texture/Flat surfaces deployed on Si substrate. The parasitic absorption in the ETL was significantly reduced, and the J_{ph} increased by more than 10 mA/cm^2 compared with those of the $BaSi_2$-pn SCs in Fig. 3. The J_{ph} reached 30.23 mA/cm^2 using the front textured surface in Fig. 5(b). Next, in order to reduce the absorption in the Si substrate and to make light-trapping effect work well, we simulated n^+-AZO/p-$BaSi_2$ HJSCs in which the Si substrate was replaced by a glass substrate. The formation of high-photoresponsivity $BaSi_2$ films on glass was already demonstrated [59]. A 100-nm thick ITO layer was used as a back contact on top of the

glass substrate and 100-nm-thick Ag was set as a reflection film on the rear side of the glass. Figures 5(c,d) show the absorption spectra of the n^+-AZO/p-$BaSi_2$ HJSCs on glass. The J_{ph} is further increased by about 1 – 2 mA/cm^2 and reached a maximum of 32.06 mA/cm^2 in Fig. 5(d). We attribute this increase to the enhanced light absorption in the p-$BaSi_2$ layer owing to the light reflected back to the p-$BaSi_2$ layer because of the Ag film.

In Fig. 6 we summarize the J_{ph} as a function of p-$BaSi_2$ thickness ($t_{p\text{-}BaSi2}$) in the range of 0.02 – 10 μm. For $BaSi_2$-pn SCs, J_{ph} saturated when $t_{p\text{-}BaSi2}$ reached 3 μm, resulting in J_{ph} ~ 20 mA/cm^2. By replacing n^+-$BaSi_2$ ETL with n^+-AZO ETL, the saturated J_{ph} increased drastically to more than 30 mA/cm^2. Furthermore, by changing the surface from flat/flat to texture/flat, it increased by more than 2 mA/cm^2. By replacing the Si substrate with glass, the saturated J_{ph} did not change, but the light absorption became more efficient for small $t_{p\text{-}BaSi2}$ (< 3 μm). The $t_{p\text{-}BaSi2}$ necessary for J_{ph} to saturate was reduced to 1 μm.

Next, using ASA-7, we performed electrical simulations of this novel solar cell configuration. We simulated the ideal case with no defect properties. Input electrical parameters were shown in Table 1. Figure 7 shows the current density versus voltage (*J-V*) characteristics of three types of $BaSi_2$ solar cells. The short-circuit current density (J_{SC}) of n^+-AZO/p-$BaSi_2$ HJSCs is much larger than that of $BaSi_2$-pn SCs due to the more efficient light absorption. Furthermore, a large open circuit voltage (V_{OC}) well over 0.8 V results from n^+-AZO/p-$BaSi_2$ HJSCs. We can therefore state that the novel n^+-AZO/p-$BaSi_2$ HJSCs is a device structure in which the excellent optical properties of $BaSi_2$ as a light absorber layer can be fully utilized.

3.3 Experimental demonstration of n^+-AZO/p-$BaSi_2$ HJSCs

Based on these simulated results, we fabricated the novel n^+-AZO/p-$BaSi_2$ HJSCs. The device structure is the same as that shown in Fig. 4. Figure 8 shows the measured *J-V* characteristics under AM1.5 illumination and the internal quantum efficiency (*IQE*) spectrum for n^+-AZO/p-$BaSi_2$ HJSCs. It shows η = 0.04%, J_{SC} = 3.7 mA/cm^2, and V_{OC} = 50 mV. *IQE* exceeded 30% at

λ = 600 nm. This efficiency is almost the same as that previously obtained for $BaSi_2$-pn SCs [31]. This is the first demonstration of this novel n^+-AZO/p-$BaSi_2$ HJSCs.

3.4 Investigation of the defect properties existing in the SCs

In Fig. 9(a) we compare the experimental and the simulated *J-V* characteristics, noting that the η of the fabricated solar cell is much smaller than that expected from the simulations. To explain the experimental results, we performed electrical simulation modelling different defect profiles. As density of states (DOS) distribution, we used conduction band tail (CBT), valence band tail (VBT), and localized states within the forbidden band gap, as shown in Fig. 9(b). The standard model of the DOS distribution consists of a parabolic conduction band (CB) and a parabolic valence band (VB), an exponentially decaying CBT and VBT. Localized states in the forbidden band gap consist of a donor-like state, the so-called $DB^{+/0}$, and an acceptor-like state, so-called $DB^{0/-}$, and are therefore represented by two energy levels $E^{+/0}$ and $E^{0/-}$ in the band diagram, respectively [60]. These energy levels are called the transition energy levels. The transition energy levels are separated from each other by a correlation energy U_{corr}.

In these electrical simulations, we first attempted to find the key parameters significantly affecting the solar cell performance and then we fine-tuned the values. We assumed that the i-ZnO layers would electrically contact the p-$BaSi_2$ layers despite the presence of the a-Si layer in between. This is because the a-Si layer is very thin and is likely to be damaged during the sputtering of i-ZnO layers. Therefore, the values of E_g and electron affinity ($q\chi$) of a-Si was set to be the same as those of $BaSi_2$. The parameters used for each layer which reproduced well the experimental result are summarized in Table 2. The most influential parameter of all was found to be the localized state density in the p-$BaSi_2$ light absorber layer ($N_{T,BaSi2}$). Figure 10(a-f) shows the dependence of $N_{T,BaSi2}$ on the *J-V* characteristic, DOS, J_{sc}, V_{oc}, η, and fill factor (*FF*), respectively. The defect level in the p-$BaSi_2$ layer is located at 0.55 eV from the CBM as shown in Fig. 10(b). As the $N_{T,BaSi2}$ was increased from 10^{12} to 10^{18} cm^{-3},

the J_{SC}, V_{OC}, and η started to sharply decrease especially when $N_{T,BaSi2} > 10^{13}$ cm^{-3}. Properties of defects in $BaSi_2$ have been investigated by various methods such as Raman spectroscopy, photoluminescence, deep-level transient spectroscopy, positron annihilation spectroscopy, and electron paramagnetic resonance [23,61–65]. It was reported that most of the defects are related to V_{Si}. A $N_{T,BaSi2}$ value of 8.8×10^{16} cm^{-3} which is reproduced well the experimental result as shown in Fig. 10(b), is much higher than that obtained by experiment in case of $BaSi_2$ epitaxial films on Si(111)(~ 10^{16} cm^{-3}) [23]. In the solar cell structure, however, the lightly B-doped p-$BaSi_2$ absorber layer was grown on the defective heavily B-doped p^+-$BaSi_2$ layer. Therefore, the $N_{T,BaSi2}$ in lower quality p-$BaSi_2$ absorber layer is likely to increase compared to that directly grown on a Si(111) substrate. In our previous work [66], a few tens of nanometer diameter B clusters were found to form in heavily B-doped p-$BaSi_2$ films, and therefore defects such as dislocations due to B clusters are present in the p-$BaSi_2$ absorber layers. Such a deep defect level can thus be attributed to the defects coming from B clusters in the heavily B-doped p^+-$BaSi_2$ underlayer. We therefore speculate that reducing the B concentration in the p^+-$BaSi_2$ layer might be effective to reduce the defect density in the p-$BaSi_2$ absorber layer. Regarding the V_{OC}, however, a small value of V_{OC} = 0.05 V cannot be explained by $N_{T,BaSi2}$ alone. As shown in Fig. 10(a), the reduction of V_{OC} was limited down to 0.6 V even at $N_{T,BaSi2} = 10^{18}$ cm^{-3}, which is still far from the experimentally obtained V_{OC}. We thus consider another factor, the shunt resistance (R_{SH}). Figure 11(a) shows the depth profiles of electron and hole concentrations under illumination in n^+-AZO/p-$BaSi_2$ HJCS with $N_{T,BaSi2} = 8.8 \times 10^{16}$ cm^{-3} at a forward bias voltage (V_{bias}) of 0.7 V, close to V_{OC}. The black-colored *J*-*V* plot in Fig. 11(b) corresponds to this solar cell. Due to large CB and VB discontinuities at the i-ZnO/p-$BaSi_2$ interface, electrons and holes accumulate at the interface, leading to the recombination of these carriers. To reflect this effect, we introduced R_{SH} in the equivalent circuit (Fig. 11(b)), and set R_{SH} to be in the range between 10^3 and 10^5 Ω. V_{OC} decreased with decreasing R_{SH} as shown in Fig. 11(b) and approached the experimental result. Finally, we summarize the *J*-*V* characteristics of n^+-AZO/p-$BaSi_2$ HJSCs

with defect properties in Fig. 12(a). All the parameters are summarized in Table 2. By reflecting the introduced defect characteristics, the simulated *J-V* characteristics perfectly matched the experimental result in Fig. 12(a). The complete DOS distribution of the p-$BaSi_2$ absorber layer is shown in Fig. 12(b).

It is noted that we need to suppress the carrier recombination to achieve a larger V_{OC} as discussed above. Theoretical analysis of the effect of band offsets at window/absorber interfaces has been made on CIS solar cells [67]. Band offsets are caused by the difference in $q\chi$ between the $BaSi_2$ absorber and the window layer. The point is to insert an interlayer to separate electrons from holes spatially. We therefore turn out attention to materials such as $Zn_{1-x}Ge_xO$ [68] whose $q\chi$ is close to that of $BaSi_2$ (3.2 eV) [69], but still tunable, likewise E_g, from 3.3 to 5.9 eV and 2.5 to 4.3 eV, respectively, by changing the Ge content *x*. Figures 13(a-c) and (a'-c') show the band diagrams and carrier concentration profiles of n^+-AZO($q\chi$ = 4.3 eV)/i-ZnO($q\chi$ = 4.3 eV)/p-$BaSi_2$($q\chi$ = 3.2 eV) and n^+-AZO($q\chi$ = 4.3 eV)/i-$Zn_{1-x}Ge_xO$($q\chi$ = 3.2 eV)/p-$BaSi_2$($q\chi$ = 3.2 eV) HJSCs, respectively, under illumination. The band diagrams were evaluated at V_{bias} = 0 V and 0.7 V, with the latter value close to that of the V_{OC}. In the case of ZnO interlayer, the accumulation of electrons and holes occurs at the i-ZnO/p-$BaSi_2$ interface (see Fig. 13(c)). This is caused by the difference in $q\chi$ between ZnO and $BaSi_2$. In contrast, such carrier accumulation is completely suppressed by inserting the $Zn_{1-x}Ge_xO$ ($q\chi$ = 3.2 eV) interlayers in Fig. 13(c'). In Table 3, we summarize the J_{SC}, V_{OC}, *FF*, and η of $BaSi_2$-pn SCs and $BaSi_2$ HJSCs with/without $Zn_{1-x}Ge_xO$ interlayers. Such effect has actually been demonstrated in CIS solar cells. Insertion of a CdS interlayer at the interface of n^+-AZO/p-CIS solar cells resulted in spatial separation of photogenerated carriers and improved the conversion efficiency [70]. On the basis of these discussions, we can state that the insertion of interlayers with their $q\chi$'s close to that of $BaSi_2$ between n^+-AZO and p-$BaSi_2$ is a very effective means to decrease the carrier recombination and thus to improve V_{OC}.

4. CONCLUSION

We investigated device structures of $BaSi_2$ solar cells by advanced opto-electrical device modelling by means of GENPRO4 and ASA-7 software. The absorption spectra of $BaSi_2$-pn SCs on Si substrates showed that the front pyramid texture was effective in increasing the J_{ph} of the 500-nm-thick p-$BaSi_2$ absorber layer by 1.2 mA/cm^2. On the other hand, the rear-texture did not yield additional optical performance. This is mainly because the Si substrate absorbs the transmitted light. Moreover, we found that the key factor inhibiting light absorption in the p-$BaSi_2$ layer was parasitic absorption in the 20-nm-thick n^+-$BaSi_2$ ETL. To prevent the parasitic absorption, we proposed a new device structure, n^+-AZO/p-$BaSi_2$ HJSCs. By using a wide band gap ETL, the parasitic absorption reduced drastically, and the J_{ph} reached 30.23 mA/cm^2. Furthermore, by replacing Si substrate with glass substrate, the required absorber layer thickness was reduced to 1 μm. Based on these simulated results, we demonstrated the first operation of n^+-AZO/p-$BaSi_2$ HJSCs experimentally. The *J-V* characteristics showed $\eta = 0.04\%$, J_{SC} = 3.7 mA/cm^2, and V_{OC} = 50 mV. *IQE* exceeded 30% at λ = 600 nm. The defects-based electrical model well reproduced the experimentally obtained *J-V* characteristics. According to the simulation results, the defect level of the p-$BaSi_2$ absorber layer was located at 0.55 eV from the CBM and its density was 8.8×10^{16} cm^{-3}, probably caused by the defective p^+-$BaSi_2$ underlayer. We also found that the carriers recombination at the heterointereface caused by carrier accumulation due to large band offsets decreased the V_{OC} significantly. An interlayer material such as $Zn_{1-x}Ge_xO$ with its $q\chi$ close to that of $BaSi_2$ placed in between the n^+-AZO and the p-$BaSi_2$ suppresses such carrier accumulation, drastically improving the V_{OC}.

ACKNOWLEDGMENTS

This work was financially supported by Japan Society for the Promotion of Science (JSPS) KAKENHI (Grant No. 18H03767). One of the authors (Y.Y.) was financially supported by a Grant-in-Aid for JSPS Fellows (No. 19J21372). We express our thanks to Dr. S. Ishizuka of

National Institute of Advanced Industrial Science and Technology, Japan, for this help in the formation of n^+-AZO layers.

References

[1] R.R. King, D. Bhusari, D. Larrabee, X.-Q. Liu, E. Rehder, K. Edmondson, H. Cotal, R.K. Jones, J.H. Ermer, C.M. Fetzer, D.C. Law, N.H. Karam, Solar cell generations over 40% efficiency, Prog. Photovolt. 20 (2012) 801–815.

[2] M. Baba, K. Makita, H. Mizuno, H. Takato, T. Sugaya, N. Yamada, Feasibility study of two-terminal tandem solar cells integrated with smart stack, areal current matching, and low concentration, Prog. Photovolt. 25 (2017) 255–263.

[3] T. Feurer, P. Reinhard, E. Avancini, B. Bissig, J. Löckinger, P. Fuchs, R. Carron, T.P. Weiss, J. Perrenoud, S. Stutterheim, S. Buecheler, A.N. Tiwari, Progress in thin film CIGS photovoltaics - Research and development, manufacturing, and applications, Prog. Photovolt. 25 (2017) 645–667.

[4] M.A. Green, A. Ho-Baillie, H.J. Snaith, The emergence of perovskite solar cells, Nat. Photonics. 8 (2014) 506–514.

[5] Y. Rong, Y. Hu, A. Mei, H. Tan, M.I. Saidaminov, S.I. Seok, M.D. McGehee, E.H. Sargent, H. Han, Challenges for commercializing perovskite solar cells, Science. 361 (2018) 1214.

[6] M. Wang, W. Li, H. Wang, K. Yang, X. Hu, K. Sun, S. Lu, Z. Zang, Small molecule modulator at the interface for efficient perovskite solar cells with high short‐circuit current density and hysteresis free, Adv. Electron. Mater. 6 (2020) 2000604.

[7] J.M. Burst, J.N. Duenow, D.S. Albin, E. Colegrove, M.O. Reese, J.A. Aguiar, C.-S. Jiang, M.K. Patel, M.M. Al-Jassim, D. Kuciauskas, S. Swain, T. Ablekim, K.G. Lynn, W.K. Metzger, CdTe solar cells with open-circuit voltage breaking the 1 V barrier, Nature Energy. 1 (2016) 16015.

[8] R. Yang, D. Wang, M. Jeng, K. Ho, D. Wang, Stable CdTe thin film solar cells with a MoOx back-contact buffer layer, Prog. Photovolt. 24 (2016) 59–65.

[9] Sb Y. Cao, X. Zhu, H. Chen, X. Zhang, J. Zhou, Z. Hu, J. Pang, Towards high efficiency inverted Sb_2Se_3 thin film solar cells, Sol. Energy Mater. Sol. Cells 200 (2019) 109945.

[10] T. Kuwano, R. Katsube, K. Kazumi, Y. Nose, Performance enhancement of $ZnSnP_2$ solar cells by a Cu_3P buffer layer, Sol. Energy Mater. Sol. Cells 221 (2021) 110891.

[11] T. Suemasu, N. Usami, Exploring the potential of semiconducting $BaSi_2$ for thin-film solar cell applications, J. Phys. D Appl. Phys. 50 (2016) 023001.

[12] K. Toh, T. Saito, T. Suemasu, Optical absorption properties of $BaSi_2$ epitaxial films grown on a transparent silicon-on-insulator substrate using molecular beam epitaxy, Jpn. J. Appl. Phys. 50 (2011) 068001.

[13] D.B. Migas, V.L. Shaposhnikov, V.E. Borisenko, Isostructural $BaSi_2$, $BaGe_2$ and $SrGe_2$: electronic and optical properties, Phys. Stat. Sol. (b). 244 (2007) 2611–2618.

[14] M. Kumar, N. Umezawa, M. Imai, $(Sr,Ba)(Si,Ge)_2$ for thin-film solar-cell applications: First-principles study, J. Appl. Phys. 115 (2014) 203718.

[15] M. Kumar, N. Umezawa, M. Imai, $BaSi_2$ as a promising low-cost, earth-abundant material with large optical activity for thin-film solar cells: A hybrid density functional study, Appl. Phys. Express 7 (2014) 071203.

[16] M. Baba, K. Toh, K. Toko, N. Saito, N. Yoshizawa, K. Jiptner, T. Sekiguchi, K.O. Hara, N. Usami, T. Suemasu, Investigation of grain boundaries in $BaSi_2$ epitaxial films on Si(111) substrates using transmission electron microscopy and electron-beam-induced current technique, J. Cryst. Growth. 348 (2012) 75–79.

[17] R.A. McKee, F.J. Walker, J.R. Conner, R. Raj, $BaSi_2$ and thin film alkaline earth silicides on silicon, Appl. Phys. Lett. 63 (1993) 2818–2820.

[18] D. Tsukahara, S. Yachi, H. Takeuchi, R. Takabe, W. Du, M. Baba, Y. Li, K. Toko, N. Usami, T. Suemasu, p-$BaSi_2$/n-Si heterojunction solar cells with conversion efficiency reaching 9.0%, Appl. Phys. Lett. 108 (2016) 152101.

[19] S. Yachi, R. Takabe, H. Takeuchi, K. Toko, T. Suemasu, Effect of amorphous Si capping layer on the hole transport properties of $BaSi_2$ and improved conversion efficiency approaching 10% in p-$BaSi_2$/n-Si solar cells, Appl. Phys. Lett. 109 (2016) 072103.

[20] T. Deng, T. Sato, Z. Xu, R. Takabe, S. Yachi, Y. Yamashita, K. Toko, T. Suemasu, p-$BaSi_2$/n-Si heterojunction solar cells on Si (001) with conversion efficiency approaching 10%: comparison with Si (111), Appl. Phys. Express 11 (2018) 062301.

[21] T. Suemasu, Exploring the possibility of semiconducting $BaSi_2$ for thin-film solar cell applications, Jpn. J. Appl. Phys. 54 (2015) 07JA01.

[22] Y. Imai, A. Watanabe, Assessment of the possibility of band gap widening of $BaSi_2$ by incorporation of carbon, Intermetallics 18 (2010) 1432–1436.

[23] Y. Yamashita, Y. Takahara, T. Sato, K. Toko, A. Uedono, T. Suemasu, Simple way of finding Ba to Si deposition rate ratios for high photoresponsivity in $BaSi_2$ films by Raman spectroscopy, Appl. Phys. Express 12 (2019) 055506.

[24] Y. Yamashita, T. Sato, N. Saitoh, N. Yoshizawa, K. Toko, T. Suemasu, Three-step growth of highly photoresponsive $BaSi_2$ light absorbing layers with uniform Ba to Si atomic ratios, J. Appl. Phys. 126 (2019) 215301.

[25] S. Sugiyama, Y. Yamashita, K. Toko, T. Suemasu, Influence of Ba-to-Si deposition rate ratios on the electrical and optical properties of B-doped $BaSi_2$ epitaxial films, Jpn. J. Appl. Phys. 59 (2020) SFFA04.

[26] S. Aonuki, Y. Yamashita, K. Toko, T. Suemasu, Fabrication of As-doped n-type $BaSi_2$ epitaxial films grown by molecular beam epitaxy, Jpn. J. Appl. Phys. 59 (2020) SFFA01.

[27] Z. Xu, D.A. Shohonov, A.B. Filonov, K. Gotoh, T. Deng, S. Honda, K. Toko, N. Usami, D.B. Migas, V.E. Borisenko, T. Suemasu, Marked enhancement of the photoresponsivity and minority-carrier lifetime of $BaSi_2$ passivated with atomic hydrogen, Phys. Rev. Mater. 3 (2019) 065403.

[28] Z. Xu, T. Sato, L. Benincasa, Y. Yamashita, T. Deng, K. Gotoh, K. Toko, N. Usami, A.B. Filonov, D.B. Migas, D.A. Shohonov, T. Suemasu, Atomic hydrogen passivation for photoresponsivity enhancement of boron-doped p-$BaSi_2$ films and performance improvement of boron-doped p-$BaSi_2$/n-Si heterojunction solar cells, J. Appl. Phys. 127 (2020) 233104.

[29] Z. Xu, T. Sato, J. Nakamura, A. Koda, K. Shimomura, A.B. Filonov, D.B. Migas, T. Suemasu, Hydrogen states in hydrogen-passivated semiconducting barium disilicide measured via muon spin rotation, Jpn. J. Appl. Phys. 59 (2020) 071004.

[30] S. Aonuki, Y. Yamashita, T. Sato, Z. Xu, K. Gotoh, K. Toko, Y. Terai, N. Usami, T. Suemasu, Significant enhancement of photoresponsivity in As-doped n-$BaSi_2$ epitaxial films by atomic hydrogen passivation, Appl. Phys. Express 13 (2020) 051001.

[31] K. Kodama, Y. Yamashita, K. Toko, T. Suemasu, Operation of $BaSi_2$ homojunction solar cells on p -Si(111) substrates and the effect of structure parameters on their performance, Appl. Phys. Express 12 (2019) 041005.

[32] Deng T, *Ph.D Thesis, Graduate School of Pure and Applied Sciences, University of Tsukuba* (2019).

[33] T. Mishima, M. Taguchi, H. Sakata, E. Maruyama, Development status of high-efficiency HIT solar cells, Sol. Energy Mater. Sol. Cells 95 (2011) 18–21.

[34] Y. Tsunomura, Y. Yoshimine, M. Taguchi, T. Baba, T. Kinoshita, H. Kanno, H. Sakata, E. Maruyama, M. Tanaka, Twenty-two percent efficiency HIT solar cell, Sol. Energy Mater. Sol. Cells 93 (2009) 670–673.

[35] N. Dwivedi, S. Kumar, A. Bisht, K. Patel, S. Sudhakar, Simulation approach for optimization of device structure and thickness of HIT solar cells to achieve ~27% efficiency, Solar Energy 88 (2013) 31–41.

[36] K. Yoshikawa, H. Kawasaki, W. Yoshida, T. Irie, K. Konishi, K. Nakano, T. Uto, D. Adachi, M. Kanematsu, H. Uzu, K. Yamamoto, Silicon heterojunction solar cell with interdigitated back contacts for a photoconversion efficiency over 26%, Nature Energy 2 (2017) 17032.

[37] Y. Chen, D. Chen, C. Liu, Z. Wang, Y. Zou, Y. He, Y. Wang, L. Yuan, J. Gong, W. Lin, X. Zhang, Y. Yang, H. Shen, Z. Feng, P.P. Altermatt, P.J. Verlinden, Mass production of industrial tunnel oxide passivated contacts (i-TOPCon) silicon solar cells with average efficiency over 23% and modules over 345 W, Prog. Photovolt. 27 (2019) 827–834.

[38] F. Feldmann, M. Bivour, C. Reichel, M. Hermle, S.W. Glunz, Passivated rear contacts for high-efficiency n-type Si solar cells providing high interface passivation quality and excellent transport characteristics, Sol. Energy Mater. Sol. Cells 120 (2014) 270–274.

[39] A. Ingenito, G. Limodio, P. Procel, G. Yang, H. Dijkslag, O. Isabella, M. Zeman, Silicon solar cell architecture with front selective and rear full area ion-implanted passivating contacts, Solar RRL. 1 (2017) 1700040.

[40] C. Hollemann, F. Haase, S. Schäfer, J. Krügener, R. Brendel, R. Peibst, 26.1%-efficient POLO-IBC cells: Quantification of electrical and optical loss mechanisms, Prog. Photovolt. 27 (2019) 950–958.

[41] G. Yang, P. Guo, P. Procel, G. Limodio, A. Weeber, O. Isabella, M. Zeman, High-efficiency black IBC c-Si solar cells with poly-Si as carrier-selective passivating contacts, Sol. Energy Mater. Sol. Cells 186 (2018) 9–13.

[42] A. Blakers, Development of the PERC Solar Cell, IEEE Journal of Photovoltaics 9 (2019) 629–635.

[43] P. Procel, G. Yang, O. Isabella, M. Zeman, Theoretical evaluation of contact stack for high efficiency IBC-SHJ solar cells, Sol. Energy Mater. Sol. Cells 186 (2018) 66–77.

[44] P. Procel, G. Yang, O. Isabella, M. Zeman, Numerical Simulations of IBC Solar Cells Based on Poly-Si Carrier-Selective Passivating Contacts, IEEE Journal of Photovoltaics 9 (2019) 374–384.

[45] R. Santbergen, T. Meguro, T. Suezaki, G. Koizumi, K. Yamamoto, M. Zeman, GenPro4 Optical Model for Solar Cell Simulation and Its Application to Multijunction Solar Cells, IEEE Journal of Photovoltaics. 7 (2017) 919–926.

[46] M. Zeman, O. Isabella, S. Solntsev, K. Jäger, Modelling of thin-film silicon solar cells, Sol. Energy Mater. Sol. Cells. 119 (2013) 94–111.

[47] https://asa.ewi.tudelft.nl/

[48] R. Takabe, S. Yachi, D. Tsukahara, K. Toko, T. Suemasu, Growth of $BaSi_2$ continuous films on Ge(111) by molecular beam epitaxy and fabrication of p-$BaSi_2$/n-Ge heterojunction solar cells, Jpn. J. Appl. Phys. 56 (2017) 05DB02.

[49] A. Ingenito, O. Isabella, S. Solntsev, M. Zeman, Accurate opto-electrical modeling of multi-crystalline silicon wafer-based solar cells, Sol. Energy Mater. Sol. Cells. 123 (2014) 17–29.

[50] MeiKei Ieong, P.M. Solomon, S.E. Laux, H. -. P. Wong, D. Chidambarrao, Comparison of raised and Schottky source/drain MOSFETs using a novel tunneling contact model, in: International Electron Devices Meeting 1998. Technical Digest (Cat. No.98CH36217), (1998) 733–736.

[51] E.O. Kane, Theory of Tunneling, J. Appl. Phys. 32 (1961) 83–91.

[52] F. Jiménez-Molinos, F. Gámiz, A. Palma, P. Cartujo, J.A. López-Villanueva, Direct and trap-assisted elastic tunneling through ultrathin gate oxides, J. Appl. Phys. 91 (2002) 5116–5124.

[53] W. Goes, Y. Wimmer, A.-M. El-Sayed, G. Rzepa, M. Jech, A.L. Shluger, T. Grasser, Identification of oxide defects in semiconductor devices: A systematic approach linking DFT to rate equations and experimental evidence, Microelectron. Reliab. 87 (2018) 286–320.

[54] Y. Inomata, T. Nakamura, T. Suemasu, F. Hasegawa, Epitaxial growth of semiconducting $BaSi_2$ thin films on Si (111) substrates by reactive deposition epitaxy, Jpn. J. Appl. Phys. 43 (2004) 4155.

[55] Y. Tian, A.R. Bento Montes, Ľ. Vančo, M. Čaplovičová, P. Vogrinčič, P. Šutta, L. Satrapinskyy, M. Zeman, O. Isabella, Toward $BaSi_2$/Si Heterojunction Thin-Film Solar Cells: Insights into Heterointerface Investigation, Barium Depletion, and Silicide-Mediated Silicon Crystallization, Adv. Mater. Interfaces. 7 (2020) 2000887.

[56] R. Takabe, K.O. Hara, M. Baba, W. Du, N. Shimada, K. Toko, N. Usami, T. Suemasu, Influence of grain size and surface condition on minority-carrier lifetime in undoped n-$BaSi_2$ on Si(111), J. Appl. Phys. 115 (2014) 193510.

[57] R. Takabe, S. Yachi, W. Du, D. Tsukahara, H. Takeuchi, K. Toko, T. Suemasu, Influence of air exposure duration and a-Si capping layer thickness on the performance of p-$BaSi_2$/n-Si heterojunction solar cells, AIP Adv. 6 (2016) 085107.

[58] R. Takabe, W. Du, K. Ito, H. Takeuchi, K. Toko, S. Ueda, A. Kimura, T. Suemasu, Measurement of valence-band offset at native oxide/$BaSi_2$ interfaces by hard x-ray photoelectron spectroscopy, J. Appl. Phys. 119 (2016) 025306.

[59] R. Koitabashi, T. Nemoto, Y. Yamashita, M. Mesuda, K. Toko, T. Suemasu, Formation of high-photoresponsivity $BaSi_2$ films on glass substrate by radio-frequency sputtering for solar cell applications, J. Phys. D Appl. Phys. 54 (2021) 135106.

[60] H. Okamoto, Y. Hamakawa, Electronic behaviors of the gap states in amorphous semiconductors, Solid State Commun. 24 (1977) 23–27.

[61] Y. Yamashita, T. Sato, M.E. Bayu, K. Toko, T. Suemasu, Investigation of electrically active defects in undoped $BaSi_2$ light absorber layers using deep-level transient spectroscopy, Jpn. J. Appl. Phys. 57 (2018) 075801.

[62] T. Sato, H. Hoshida, R. Takabe, K. Toko, Y. Terai, T. Suemasu, Detection of local vibrational modes induced by intrinsic defects in undoped $BaSi_2$ light absorber layers using Raman spectroscopy, J. Appl. Phys. 124 (2018) 025301.

[63] T. Sato, Y. Yamashita, Z. Xu, K. Toko, S. Gambarelli, M. Imai, T. Suemasu, Correlation of native defects between epitaxial films and polycrystalline $BaSi_2$ bulks based on photoluminescence spectra, Appl. Phys. Express 12 (2019) 111001.

[64] T. Sato, C. Lombard, Y. Yamashita, Z. Xu, L. Benincasa, K. Toko, S. Gambarelli, T. Suemasu, Investigation of native defects in $BaSi_2$ epitaxial films by electron paramagnetic resonance, Appl. Phys. Express 12 (2019) 061005.

[65] A. Montes, S.W.H. Eijt, Y. Tian, R. Gram, H. Schut, T. Suemasu, N. Usami, M. Zeman, J. Serra, O. Isabella, Point defects in $BaSi_2$ thin films for photovoltaic applications studied by positron annihilation spectroscopy, J. Appl. Phys. 127 (2020) 085304.

[66] M. Ajmal Khan, K. Nakamura, W. Du, K. Toko, N. Usami, T. Suemasu, Precipitation control and activation enhancement in boron-doped p^+-$BaSi_2$ films grown by molecular beam epitaxy, Appl. Phys. Lett. 104 (2014) 252104.

[67] T. Minemoto, T. Matsui, H. Takakura, Y. Hamakawa, T. Negami, Y. Hashimoto, T. Uenoyama, M. Kitagawa, Theoretical analysis of the effect of conduction band offset of window/CIS layers on performance of CIS solar cells using device simulation, Sol. Energy Mater. Sol. Cells 67 (2001) 83–88.

[68] T. Minami, Y. Nishi, T. Miyata, Efficiency enhancement using a $Zn_{1-x}Ge_xO$ thin film as an n-type window layer in Cu_2O-based heterojunction solar cells, Appl. Phys. Express 9 (2016) 052301.

[69] T. Suemasu, K. Morita, M. Kobayashi, M. Saida, M. Sasaki, Band Diagrams of $BaSi_2$/Si Structure by Kelvin Probe and Current-Voltage Characteristics, Jpn. J. Appl. Phys. 45 (2006) L519–L521.

[70] L. Stolt, J. Hedström, J. Kessler, M. Ruckh, K. Velthaus, H. Schock, ZnO/CdS/$CuInSe_2$ thin‐film solar cells with improved performance, Appl. Phys. Lett. 62 (1993) 597−599.

Table. 1: Input electrical parameters of each layer used for ideal simulation.

	n^+-AZO	ZnO	a-Si	n-$BaSi_2$	p-$BaSi_2$	p^+-$BaSi_2$
E_g [eV]	3.3	3.3	1.3	1.3	1.3	1.3
$q\chi$ [eV]	3.5	3.5	3.2	3.2	3.2	3.2
N_C [cm^{-3}]	3.0×10^{18}	3.0×10^{18}	2.0×10^{20}	2.6×10^{19}	2.6×10^{19}	2.6×10^{19}
N_V [cm^{-3}]	1.7×10^{19}	1.7×10^{19}	2.0×10^{20}	2.0×10^{19}	2.0×10^{19}	2.0×10^{19}
ε	9	9	11.9	14	14	14
n/p [cm^{-3}]	1.0×10^{20}	1.0×10^{17}	9.7×10^{15}	1.0×10^{19}	1.0×10^{17}	2.0×10^{19}
μ_e [$cm^2 V^{-1}s^{-1}$]	50	50	5	500	800	500
μ_h [$cm^2 V^{-1}s^{-1}$]	31	31	1	30	100	30

Table 2: Input electrical and defective parameters used for each layer which reproduced well the experimental result.

	n^+-AZO	ZnO	a-Si	p-$BaSi_2$	p^+-$BaSi_2$
E_g [eV]	3.3	3.3	1.3	1.3	1.3
$q\chi$ [eV]	3.5	3.5	3.2	3.2	3.2
N_C [cm^{-3}]	3.0×10^{18}	3.0×10^{18}	2.0×10^{20}	2.6×10^{19}	2.6×10^{19}
N_V [cm^{-3}]	1.7×10^{19}	1.7×10^{19}	2.0×10^{20}	2.0×10^{19}	2.0×10^{19}
ε	9	9	11.9	14	14
n/p [cm^{-3}]	1.0×10^{17}	1.0×10^{17}	9.7×10^{15}	8.0×10^{16}	1.0×10^{18}
μ_e [$cm^2\,V^{-1}s^{-1}$]	50	50	5	800	500
μ_h [$cm^2\,V^{-1}s^{-1}$]	31	31	1	77	30
Hole capture rate in VBT [$m^{-3}s^{-1}$]	1.0×10^{-19}	1.0×10^{-19}	1.0×10^{-17}	1.0×10^{-15}	1.0×10^{-15}
Electron capture rate in VBT [$m^{-3}s^{-1}$]	5.0×10^{-17}	5.0×10^{-17}	1.0×10^{-15}	1.0×10^{-15}	1.0×10^{-15}
DOS in VBT [$m^{-3}eV^{-1}$]	1.0×10^{25}	1.0×10^{25}	1.0×10^{25}	1.0×10^{25}	1.2×10^{24}
Slope of the VBT [eV]	0.01	0.01	0.044	0.02	0.1
Hole capture rate in CBT [$m^{-3}s^{-1}$]	1.0×10^{-19}	1.0×10^{-19}	1.0×10^{-17}	1.0×10^{-15}	1.0×10^{-15}
Electron capture rate in CBT [$m^{-3}s^{-1}$]	1.0×10^{-19}	1.0×10^{-19}	1.0×10^{-15}	1.0×10^{-15}	1.0×10^{-15}
DOS in CBT [$m^{-3}eV^{-1}$]	1.0×10^{25}	1.0×10^{25}	1.0×10^{25}	1.0×10^{25}	1.2×10^{24}
Slope of the CBT [eV]	0.01	0.01	0.03	0.02	0.1
U_{corr} [eV]	0.2	0.2	0	0.1	0
Electron capture rate of neutral DB [$m^{-3}s^{-1}$]	1.0×10^{-17}	1.0×10^{-17}	1.0×10^{-10}	1.0×10^{-11}	1.0×10^{-11}
Electron capture rate of positive DB [$m^{-3}s^{-1}$]	1.0×10^{-17}	1.0×10^{-17}	1.0×10^{-10}	1.0×10^{-11}	1.0×10^{-11}
Hole capture rate of neutral DB [$m^{-3}s^{-1}$]	1.0×10^{-17}	1.0×10^{-17}	1.0×10^{-10}	1.0×10^{-11}	1.0×10^{-11}
Hole capture rate of negative DB [$m^{-3}s^{-1}$]	1.0×10^{-17}	1.0×10^{-17}	1.0×10^{-10}	1.0×10^{-11}	1.0×10^{-11}
Defect density N_T [cm^{-3}]	1.0×10^{17}	1.0×10^{15}	1.0×10^{14}	8.8×10^{16}	3.5×10^{17}
Energy relative to midgap [eV]	0.1	0.1	0.0	0.1	–0.2

Table 3: Progress in the modelling-based optimization of external parameters of different solar cells based on p-$BaSi_2$ absorber material. *Ultimate* stands for n^+-$Zn_{1-x}Ge_xO$/i-$Zn_{1-x}Ge_xO$/p-$BaSi_2$ HJSC on glass.

	$BaSi_2$-pn on Si	n^+-AZO/p-$BaSi_2$ on Si		n^+-AZO/p-$BaSi_2$ on Glass		*Ultimate*
	Flat/Flat	Flat/Flat	Tex./Flat	Flat/Flat	Tex./Flat	Tex./Flat
d_{BaSi2} [μm]	0.5	0.5	0.5	0.5	0.5	0.5
J_{SC} [mA/cm^2]	11.2	27.4	30.5	27.9	30.5	32.9
V_{OC} [V]	0.80	0.84	0.84	0.77	0.77	0.84
FF [-]	0.85	0.85	0.86	0.78	0.80	0.86
η [%]	7.6	19.6	22.0	16.7	18.9	23.9

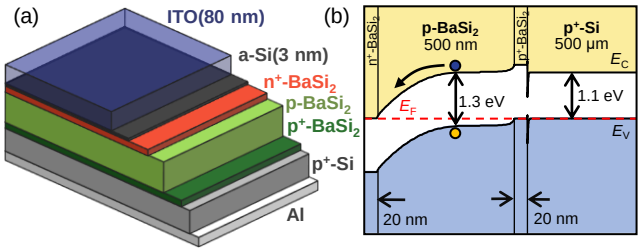

FIGURE 1 (a) Schematic image and (b) band alignment of $BaSi_2$-pn homojunction solar cells simulated by ASA-7. p-$BaSi_2$ is used as a light absorber, and photogenerated electrons flow to the n^+-$BaSi_2$ side.

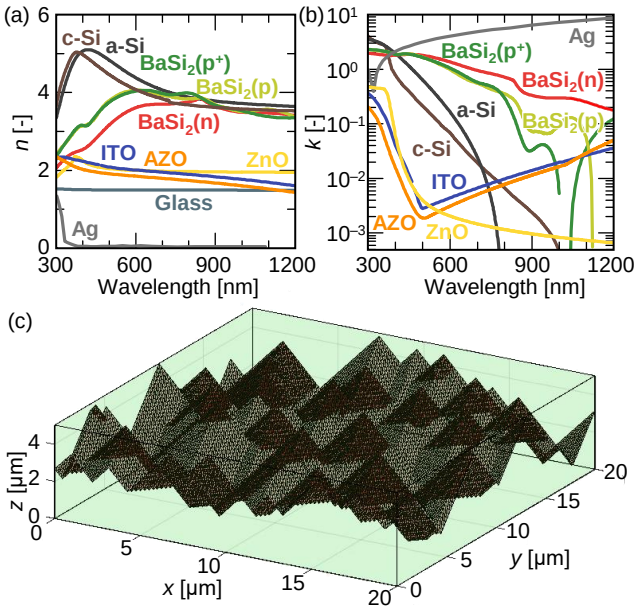

FIGURE 2 (a) Refractive index $n(\lambda)$ and (b) extinction coefficient $k(\lambda)$ of layers used for optical simulations. These data were measured by spectroscopic ellipsometry. (c) 3D pyramidal texture measured by AFM.

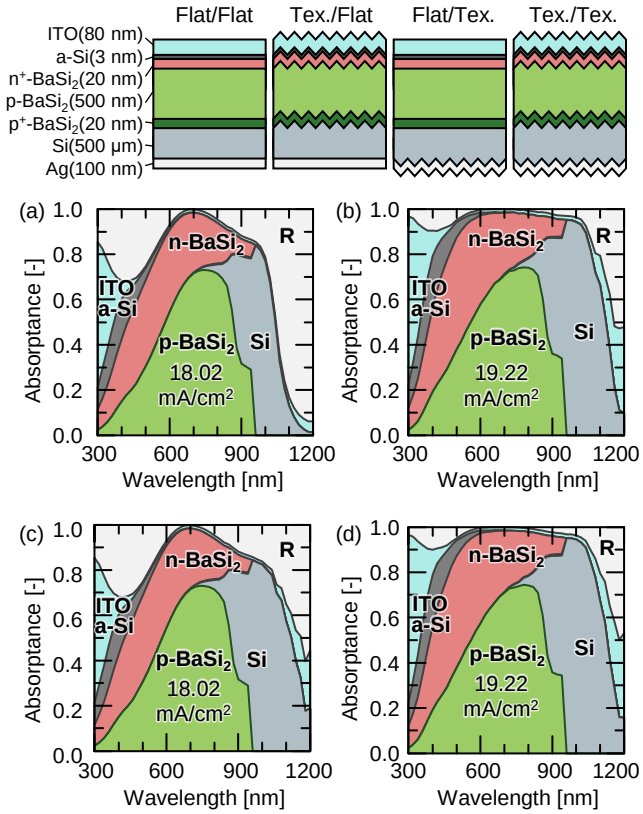

FIGURE 3 Reflection and absorption spectra of $BaSi_2$ homojunction solar cells with (a) Flat/Flat, (b) Texture/Flat, (c) Flat/Texture, (d) Texture/Texture surfaces. The photocurrent density J_{ph} generated in the p-$BaSi_2$ absorber layer is shown.

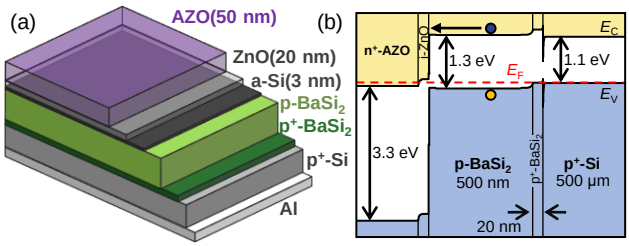

FIGURE 4 (a) Schematic and (b) band diagram of an n^+-AZO/ p-$BaSi_2$ heterojunction solar cell in equilibrium.

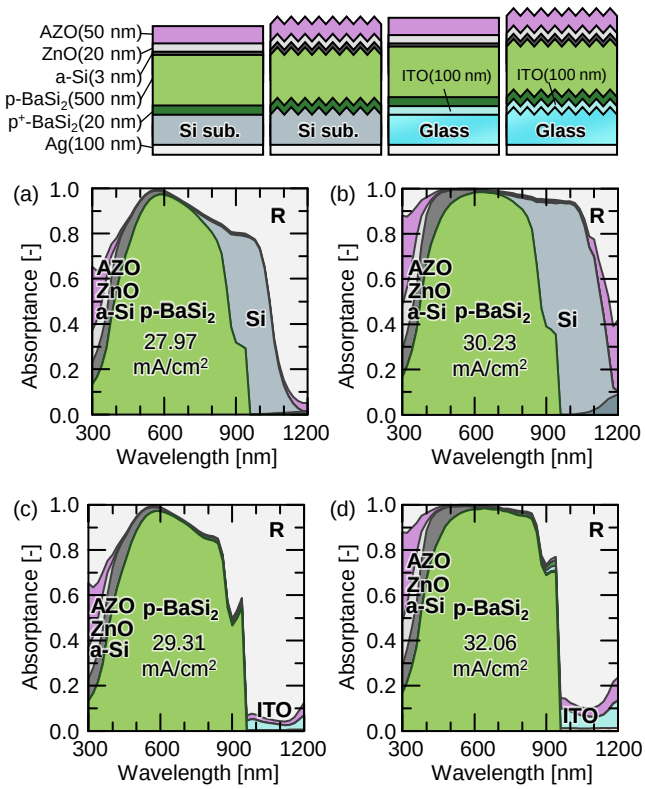

FIGURE 5 Absorption spectra of AZO/$BaSi_2$ heterojunction solar cells with (a)-(c) Flat/Flat and (b)-(d) Texture/Texture surfaces on Si or glass substrates. The photocurrent density J_{ph} generated in the p-$BaSi_2$ absorber layer is shown.

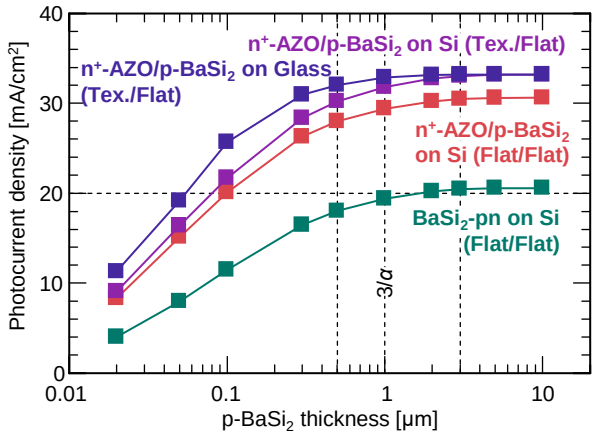

FIGURE 6 Dependence of J_{ph} on the thickness of p-$BaSi_2$ light absorber layer in four types of $BaSi_2$ solar cells (on Si substrate: flat $BaSi_2$-pn, flat n^+-AZO/p-$BaSi_2$, textured n^+-AZO/p-$BaSi_2$; on glass substrate: textured n^+-AZO/p-$BaSi_2$).

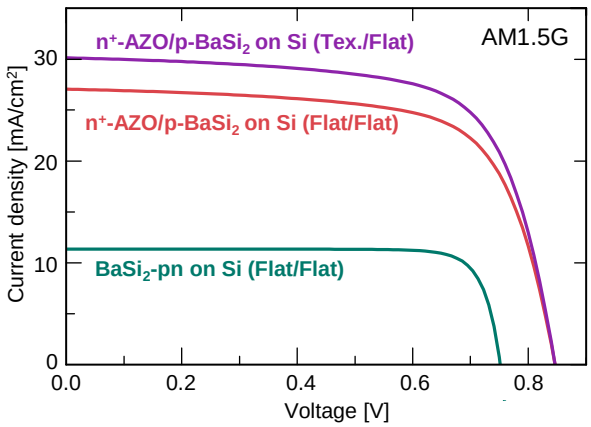

FIGURE 7 (a) *J-V* characteristics of three types of $_{BaSi2}$ solar cells (on Si substrate: flat $BaSi_2$-pn, flat n^+-AZO/p-$BaSi_2$, textured n^+-AZO/p-$BaSi_2$).

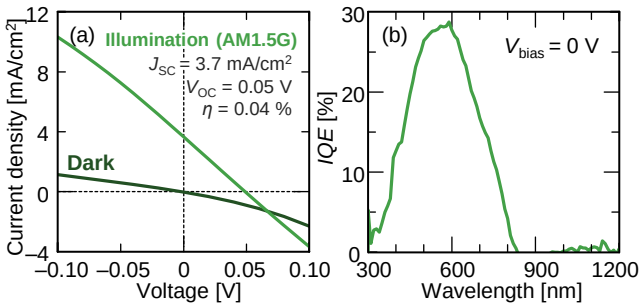

FIGURE 8 (a) *J-V* characteristics and (b) *IQE* spectrum of n^+-AZO/p-$BaSi_2$ HJSCs. The solar cell operation was demonstrated for the first time.

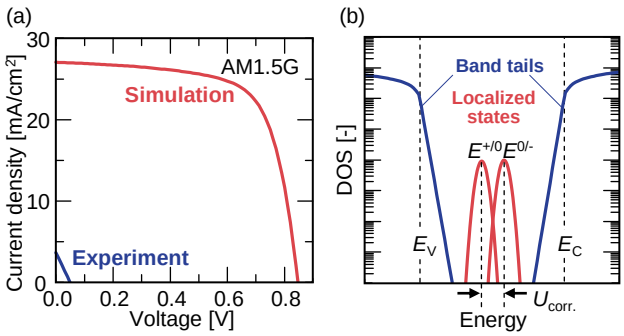

FIGURE 9 (a) Comparison of *J-V* characteristics between experimental and simulated flat n^+-AZO/p-$BaSi_2$ HJSCs; (b) Density of States distribution in p-$BaSi_2$ absorber.

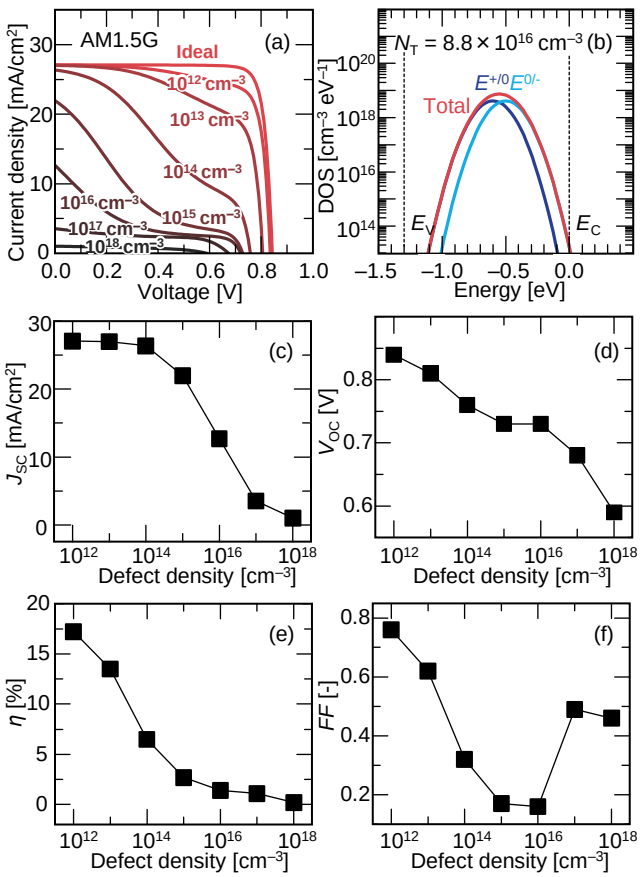

FIGURE 10 The effect of the defect density N_T in p-$BaSi_2$ light absorber. (a) *J-V* characteristics of n^+-AZO/p-$BaSi_2$ HJSCs as function of defect level in p-$BaSi_2$ absorber and (b) DOS distribution; (c-f) dependence of the defect density in p-$BaSi_2$ on J_{SC}, V_{OC}, η, and fill factor (*FF*), respectively.

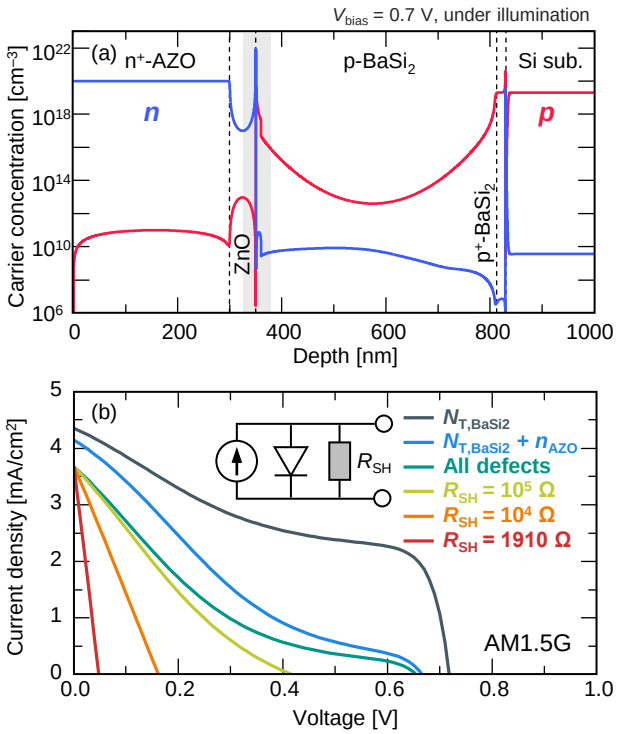

FIGURE 11 (a) The depth profile of carrier concentration in n⁺-AZO/p-$BaSi_2$ HJSCs under a forward bias voltage of 0.7 V under illumination and (b) calculated *J-V* characteristics at $N_{T,BaSi2}$ = 8.8 × 10^{16} cm^{-3} and n_{AZO} = 10^{17} cm^{-3}. By introducing shunt resistance, *J-V* profiles fitted to that obtained in experiments.

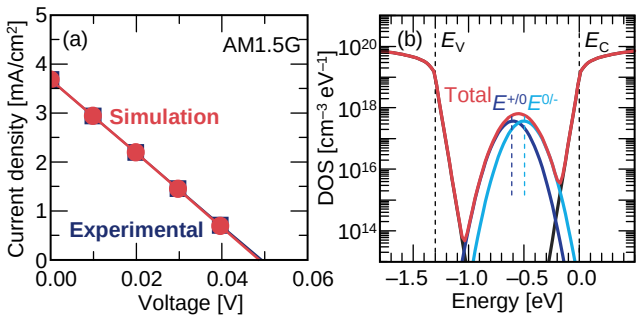

FIGURE 12 (a) *J-V* characteristics of experimental and simulated flat n^+-AZO/p-$BaSi_2$ HJSCs and (b) profiles of tailored DOS and defect levels to reproduce the experimental *J-V* characteristics in (a).

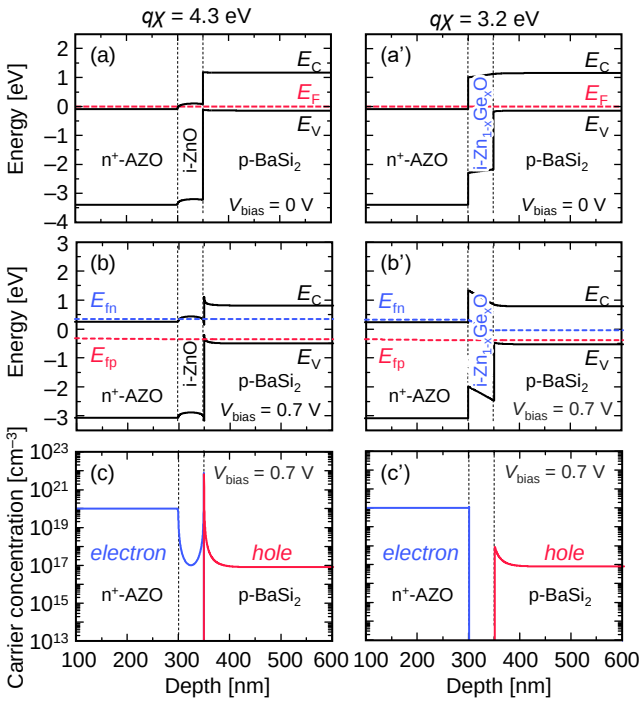

FIGURE 13 Band diagrams of n⁺-AZO/p-$BaSi_2$ HJSCs with an inter layer of qχ = (a,b) 4.3 and (a',b') 3.2 eV at V_{bias} = 0 and 0.7 V under illumination. (c,c') Depth profiles of electron and hole concentrations at V_{bias} = 0.7 V .